

# A living mesoscopic cellular automaton made of skin scales

Liana Manukyan<sup>1,2\*</sup>, Sophie A. Montandon<sup>1\*</sup>, Anamarija Fofonjka<sup>1,2\*</sup>, Stanislav Smirnov<sup>3,4,5</sup> & Michel C. Milinkovitch<sup>1,2</sup>

In vertebrates, skin colour patterns emerge from nonlinear dynamical microscopic systems of cell interactions. Here we show that in ocellated lizards a quasi-hexagonal lattice of skin scales, rather than individual chromatophore cells, establishes a green and black labyrinthine pattern of skin colour. We analysed time series of lizard scale colour dynamics over four years of their development and demonstrate that this pattern is produced by a cellular automaton (a grid of elements whose states are iterated according to a set of rules based on the states of neighbouring elements) that dynamically computes the colour states of individual mesoscopic skin scales to produce the corresponding macroscopic colour pattern. Using numerical simulations and mathematical derivation, we identify how a discrete von Neumann cellular automaton emerges from a continuous Turing reaction–diffusion system. Skin thickness variation generated by three-dimensional morphogenesis of skin scales causes the underlying reaction–diffusion dynamics to separate into microscopic and mesoscopic spatial scales, the latter generating a cellular automaton. Our study indicates that cellular automata are not merely abstract computational systems, but can directly correspond to processes generated by biological evolution.

Most vertebrates exhibit non-random spatial variation of their skin colour, that is, they present a colour pattern. Depending on the species, individual and body area, these symmetry-breaking regularities can take various forms such as stripes, spots, tessellations, meanders and labyrinths. Patterns can either be fixed at birth or change during the life of the animal. These macroscopic patterns result from sustained nonequilibrium dissipative microscopic systems that clearly involve short-range and long-range interactions among biological cells<sup>1–5</sup>. At the macroscopic scale, such dynamical processes can be approximated as involving continuous media and can be described quantitatively with nonlinear partial differential equations similar to those used in the reaction–diffusion (RD) framework<sup>6–10</sup>.

Squamates (lizards and snakes) are interesting models in which to study skin pattern development because many species exhibit a broad variety of colours and patterns. Typically, the colour of a lizard's patch of skin is the result of a combination of structural and pigmentary elements found in various types of chromatophores<sup>11–15</sup>. Iridophore cells produce structural colours through light interference (due to the presence of quasi-ordered arrays of guanine nanocrystals<sup>15</sup>), but all other chromatophores contain pigments: brown/black melanins in melanophores, yellow pteridines/carotenoids in xanthophores and red pteridines/carotenoids in erythrophores<sup>16</sup>. For example, many species of squamates (and of amphibians) use such non-trivial combinations of cell types to produce green<sup>14</sup>, one of the most ubiquitous skin colours in nature (because it blends into chlorophyll-rich environments). In many species, individuals can additionally control their brightness by dispersion or aggregation of intracellular melanin-containing organelles<sup>17–20</sup>, and several chameleon species can change colours (hue) for the purpose of social signalling through the active tuning of a three-dimensional (3D) lattice of guanine nanocrystals within iridophores<sup>15</sup>.

The development of a specific skin colour pattern is produced by a nonlinear dynamical system of biological cell interactions that simultaneously establishes the co-localization of pigmentary and structural

elements (generating a specific perceived colour) and their spatial variation (generating a pattern). However, the formation and ontogenetic dynamics of skin colour in the ocellated lizard (*Timon lepidus*) seems to conflict with this RD framework, given that mesoscopic skin scales, rather than individual chromatophore cells, establish the pattern. Indeed, the juvenile pattern is made of white ocelli on a brown background (Fig. 1a) but develops later into a labyrinthine pattern (Fig. 1b–g): each adult scale is essentially homogeneous in colour and is either green or black. Hence, the relevant dynamic occurs between the microscopic and mesoscopic scales: the (spatial) scale of (skin) scales. Note that we choose to ignore the ventral scales (which remain white throughout the life of the animal) and the development of blue ocelli on the flanks.

Here we analyse the dynamics of the skin colour pattern formation in ocellated lizards and demonstrate that this labyrinthine pattern is computed on a discrete-state dynamical lattice of mesoscopic elements (the skin scales) by a quasi-hexagonal probabilistic cellular automaton (CA). After identifying the rule of the CA, we perform continuous and discrete RD modelling to identify how a CA behaviour (at the spatial scale of skin scales) can emerge from the paradigmatic nonlinear interactions among chromatophores (at a much smaller spatial scale). Our multi-scale analyses suggest that the morphological patterning of the skin into scales generates 3D geometric variations that affect the cell interactions and cause the emergence of a CA behaviour exactly superposed on the skin scales.

Chromatophore densities obey diffusion equations but reactions among cells make the situation more intricate. It was first theoretically understood by Turing<sup>6</sup>, the implications of whose work have since been widely studied<sup>7,21</sup>, that, at some parameter values, the nonlinearity of the resulting (non-scale invariant) RD equations generates various patterns at a specific spatial scale<sup>22,23</sup>. The 3D RD dynamics in the skin layer can be projected to a two-dimensional (2D) RD equation on the surface of the skin. However, we suggest that the 3D geometry of the

<sup>1</sup>Laboratory of Artificial and Natural Evolution (LANE), Department of Genetics and Evolution, University of Geneva, Geneva, Switzerland. <sup>2</sup>SIB Swiss Institute of Bioinformatics, Geneva, Switzerland.

<sup>3</sup>Department of Mathematics, University of Geneva, Geneva, Switzerland. <sup>4</sup>Skolkovo Institute of Science and Technology, Skolkovo, Russia. <sup>5</sup>Chebyshev Laboratory, Department of Mathematics and Mechanics, St Petersburg State University, St Petersburg, Russia.

\*These authors contributed equally to this work.

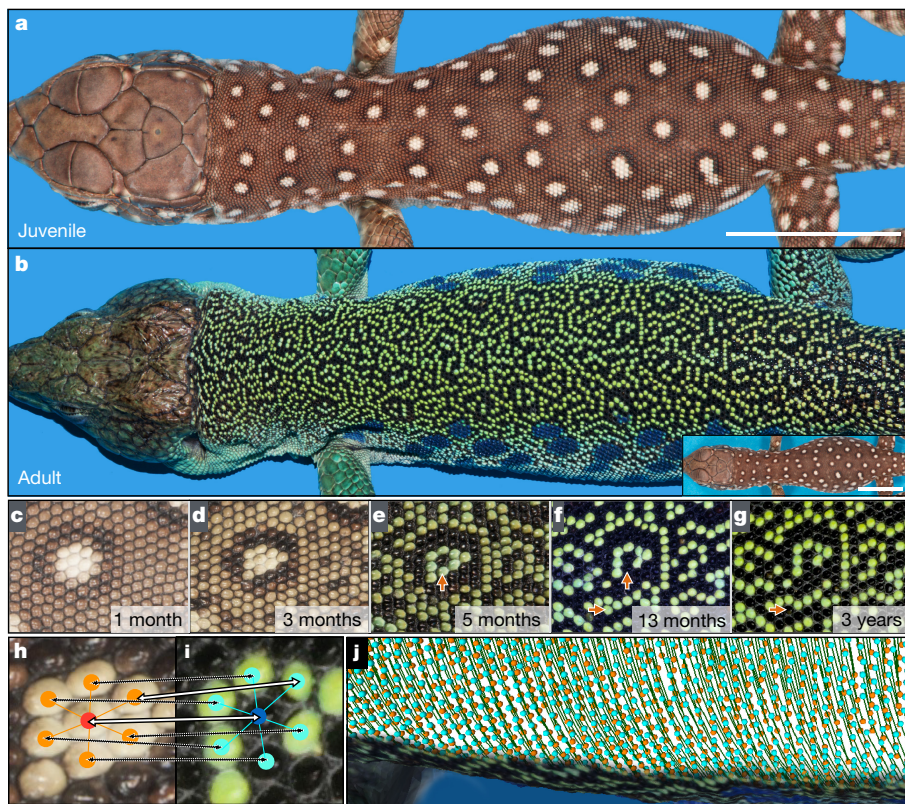


**Figure 1 | Colour pattern ontogeny in ocellated lizards.** **a, b,** The colour pattern changes drastically over about three years from the juvenile (**a**) to the adult (**b**). The inset of **b** shows a juvenile on the same spatial scale as the adult. **c–g**, Close-ups of the same individual as in **a** and **b**, illustrating the pattern time evolution at different ages. Orange arrows show two examples of colour switching between two time points. **h, i**, Principle of scales matching between time points: one scale and

one of its nearest neighbours are manually matched between the two time points (white double-headed arrows), then all remaining nearest neighbours are automatically matched using local translation, rotation and scaling factors estimated using the previously matched scales. **j**, Scale matching is automatically propagated until all scales are aligned between the two time points. Scale bars in **a** and **b** are 11 mm.

skin—that is, the presence of skin scales—changes the resulting 2D diffusion parameters at the scale border, effectively decoupling the behaviour of the 2D RD equations within and between skin scales.

We formally show that modulating RD diffusion coefficients at the scale boundaries is sufficient to mathematically derive a discrete RD model (with entire reptile scales as discretization units) from a continuous RD model. In short, the derivation implies that, within a single skin scale, parameters are such that the scale rapidly takes a uniform colour. In the diffusion term, the Laplacian is replaced by its discrete counterpart (properly renormalized), whereas the reaction term remains unchanged. Numerical analyses show that the uniform colour of a scale quickly converges to one of two extreme states (green or black) and can flip between them (quickly compared to large spatial scale changes), depending on the states of neighbour scales. Effectively, individual skin scales can be assumed monochromatic at any given time, and the macroscopic pattern consists of a lattice of black and green scales, reducing dynamics to a probabilistic CA whose corresponding probability distributions can be derived from discrete RD numerical simulations.

CAs have been extensively used for modelling continuous systems undergoing patterning<sup>24,25</sup>, with the grid elements of the CA being substantially smaller than the length scale of the generated pattern, that is, a discrete system permits a continuous one to be modelled. The phenomenon we describe here is fundamentally different: we show that the ocellated lizards' lattice of mesoscopic scales behaves as a CA that computes a macroscopic pattern. We show that this discrete system can be generated by a continuous one (modelled by RD). Our study provides evidence for a mesoscopic CA behaviour in a biological system. In other words, we show that the fundamental development, by von Neumann<sup>26,27</sup>, of CAs as computational systems (which have found

many applications<sup>28</sup>), is not just an abstract concept but corresponds to a process generated by biological evolution. The CA parameters, which probably evolved by natural selection, turn out to be in a range generating quasi-chaotic macroscopic patterns.

### Juvenile to adult pattern

To study the dynamics of scale colour change in ocellated lizards, we used a robotic high-resolution system<sup>29</sup> to perform surface scanning of three male individuals at multiple time points, from about two weeks after hatching to an age of three to four years. We reconstructed (with resolution  $<40\mu\text{m}$ ) the 3D geometry and colour texture of each animal at each time point with a combination of structure from motion (SFM<sup>30</sup>) and photometric stereo (PS<sup>31</sup>) approaches. We then performed semi-automated detection of about 5,000 dorsal scales per scan using skin texture or mean curvature information, and we retrieved first-ring neighbourhood connectivity using local 2D Voronoi diagrams with the centres of scales as the network vertices (Extended Data Fig. 1). Given that the number of scales is invariant across the lifetime of an individual, we used local rigid alignment and global non-rigid deformations to map the networks of scales across scans, that is, we obtained for each individual a scale-per-scale correspondence between developmental time points (Fig. 1h–j). Automated colour assignment of each scale at each time point was performed with a colour quantization clustering approach (see Methods) and all scale colour changes were automatically identified and visually verified.

The juvenile pattern (Fig. 1a and c) consists of about sixty white ocelli each composed of 5 to 17 scales; all other dorso-lateral scales exhibit a rather homogeneous brown colour, although they tend to be darker in the vicinity of ocelli. Gradually (and faster in males than

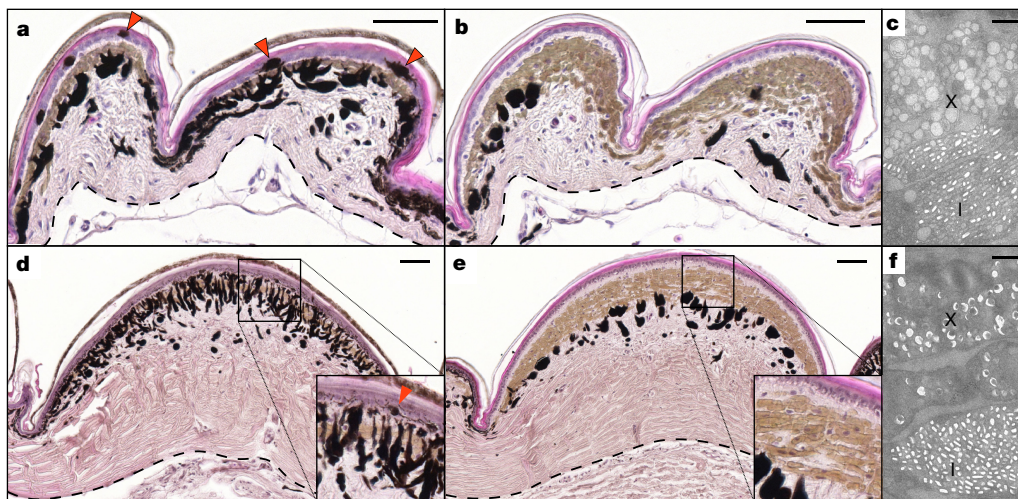


**Figure 2 | Different combinations of chromatophores generate different scale colours.** **a**, Histological section of newborn brown scales: red arrowheads indicate epidermal melanophores; dermal melanophores send short projections through the layer of iridophores (brown cells). **b**, Section of newborn white scales: the epidermis does not contain melanophores, whereas the dermis contains scarce and condensed melanophores under a thick layer of iridophores. **c**, Scanning electron microscopy indicates that white scales include xanthophores (X) with immature (unpigmented)

stage-I pterinosomes. Iridophores are indicated with I. **d**, Black scales show epidermal melanophores (arrowhead in inset) and large dermal melanophores with a dense array of dendrites extending to the dermis/epidermis border. **e**, Green scales exhibit condensed dermal melanophores under a very thick layer of iridophores (brown cells in inset). **f**, Xanthophores in green and black scales are fully differentiated (pigmented stage-III pterinosomes). Dotted lines in **a**, **b**, **d** and **e** indicate the bottom edge of the skin. Scale bars are 50  $\mu$ m in **a**, **b**, **d** and **e** and 1  $\mu$ m in **c** and **f**.

females), most white and brown scales become green but some, especially around ocelli, become black (Fig. 1d and e). Strikingly, scales continue to change colour individually, black to green and green to black (via an intermediate brownish state) throughout the life of the animal, although the rate of change decreases drastically with age. About 1,500 dorsal scales change colour over a period of four years. This causes a gradual qualitative change of the pattern: the outlines of the original ocelli become obliterated and the pattern turns into a labyrinthine assortment of contrasting black and green chains of scales (Fig. 1b, f and g; Supplementary Videos 1 and 2). The function of this adult pattern is unknown but is likely to be associated with camouflage (through disruption of the animal outline) or sexual selection<sup>17,32,33</sup>. Functional considerations are beyond the scope of this Article and we focus here on the mechanism and dynamics of pattern formation.

We analysed, using optical microscopy and transmission electron microscopy (TEM), sections of juvenile and adult skin to identify the pigmentary and structural elements producing the various colours of scales. In juveniles, brown scales contain epidermal and dermal melanophores as well as a thin layer of iridophores (Fig. 2a), whereas white scales exhibit no visible epidermal melanophores and only sparse contracted dermal melanophores under a thick layer of iridophores (Fig. 2b). We note that xanthophores are not visible in brown scales and are immature (that is, with non-fully differentiated pterinosomes; Fig. 2c) in white scales. In adults, black scales (Fig. 2d) contain sparse small epidermal melanophores as well as many dermal melanophores whose dendrites extend to the dermis/epidermis border after traversing thin layers of iridophores and of mature xanthophores. On the other hand, green scales (Fig. 2e) exhibit melanophores with their melanosomes aggregated around the cell body (pigmented dendrites never reach the epidermis border) under a thick layer of iridophores (about 50  $\mu$ m, which is 3–4 times thicker than in black scales) and a thin layer of mature xanthophores (Fig. 2f).

### Skin colour change is computed by a CA

During the transition from the juvenile to the adult pattern, the proportion of black versus green scales increases until green scales tend to exhibit four black and two green direct neighbours whereas black scales tend to have three black and three green direct neighbours (Fig. 3a and b). First, we tested whether this transition is generated by a random scale-autonomous mechanism, that is, a process by which scales change

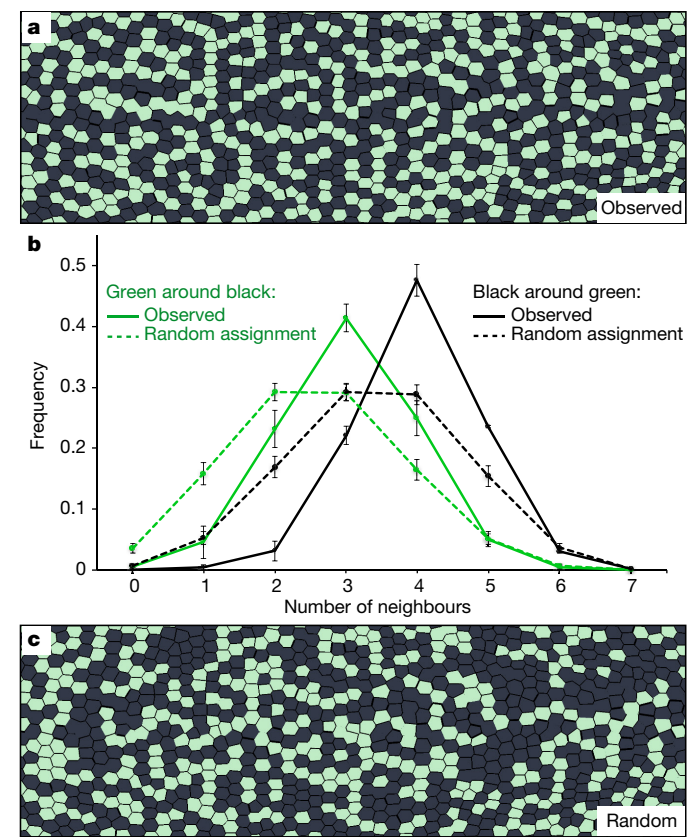


**Figure 3 | Neighbourhood distributions of real and random patterns.** **a–c**, Real patterns (such as the one in **a**) exhibit neighbourhood state distributions (solid lines in **b**) in which green and black scales tend to have four and three direct neighbours, respectively, of the opposite colour (means and standard deviations (s.d.) are shown for three adult male individuals). Neighbourhood distributions generated by scale-autonomous initializations (dotted lines in **b**; data points and error bars show means  $\pm$  s.d. among 1,000 pseudo-randomizations) with genuine green and black scale proportions are substantially different from observed distributions, and the corresponding colour patterns (**c**) exhibit clustering of same-colour scales, which is unobserved in real ocellated lizards.

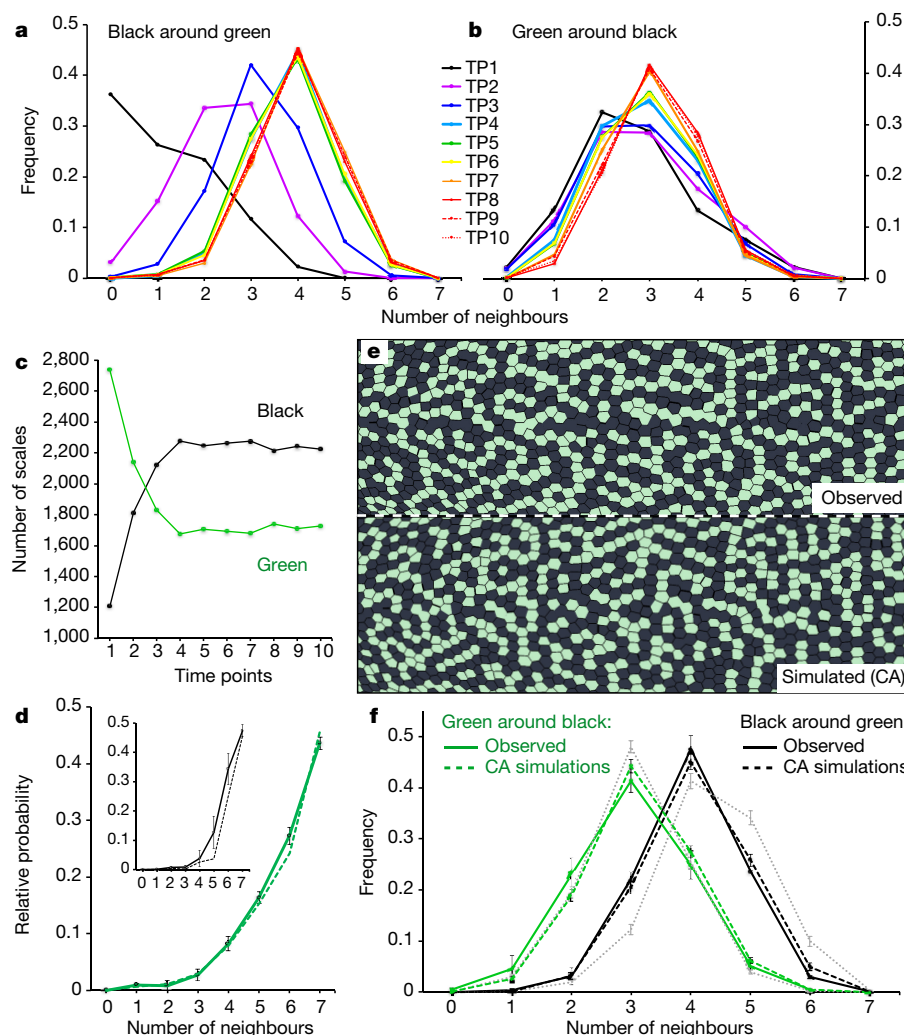


**Figure 4 | Scale colour changes follow a probabilistic CA.** a–c, During time evolution of the skin colour pattern from the juvenile to the adult (ten time points from TP1 to TP10), the number of black around green scales (a) and green around black scales (b) both increase with the age of the animal, while the proportion of black scales (c) increases to about 60%. d, Observed colour change probability distributions (mean  $\pm$  s.d. among three individuals) are very similar for different time points and different individuals. The probabilities that green scales (green line) and black scales (black line, inset) will change colour increase polynomially with the number of nearest-neighbour scales matching the initial colour (dotted green and black lines indicate the optimal probability distributions

colour independently of the state of other scales. Pseudo-random initialization of each scale to either the black or the green state, while preserving the global proportion of the two states (59% black and 41% green) clearly generates increased clustering of black scales (Fig. 3c), whereas the real pattern includes more strings of green or black scales (Fig. 3a). In addition, real versus randomly initialized patterns exhibit dramatically different scale neighbour state distributions: for example, green scales in the random pattern have far fewer black direct neighbours than in the real pattern (Fig. 3b).

As an alternative to random scale-autonomous colour change, we tested whether scale states follow a CA process, that is, whether the colour state of a scale at time  $t + 1$  is a function of the state of its neighbours at time  $t$ . The time evolution of neighbourhood state distributions indicates that the number of black scales around green scales drastically and continuously increases until the mode stabilizes at a value of four after about 14–16 months of pattern evolution (Fig. 4a), while the number of green scales around black scales increases moderately as the animal ages until its mode stabilizes at a value of three (Fig. 4b). During that

obtained with a genetic algorithm selecting for similar neighbourhood state statistics; see Methods). e, f, CA numerical simulations implementing these probabilities generate patterns (e) and neighbourhood distributions (dashed lines in f; data points are mean  $\pm$  s.d. among 1,000 simulations) undistinguishable from real patterns and real distributions (solid lines in f; data points are mean  $\pm$  s.d. among three individuals). The observed and simulated patterns (1,500 scale colour changes) are unlikely at steady state as the neighbourhood distributions continue to shift slightly (dotted grey lines in f; data points are mean  $\pm$  s.d. among 1,000 CA simulations carried out until 3,000–5,000 scales have changed colour).

process, the proportion of black scales rapidly increases from about 30% to 60% (Fig. 4c) and stabilizes around that value.

From these time series of colour changes, we computed estimates of  $p_G(n_G)$ , the probability of changing colour for a green scale with  $n_G$  first-neighbour green scales, and of  $p_B(n_B)$ , the probability of changing colour for a black scale with  $n_B$  first-neighbour black scales. Figure 4d indicates that the probability of black and green scales changing colour increases polynomially (Extended Data Fig. 2a) with the number of nearest-neighbour scales matching their colour. These probability distributions have very similar shapes among individuals as well as between different time points for a single animal (Fig. 4d and Extended Data Fig. 2b). Hence, scale colour change in ocellated lizards follows a probabilistic CA process: the probability for a scale to flip from one colour state to the other at time  $t + 1$  is a function of the state of its first neighbours at time  $t$ .

We tested the validity of the above-inferred CA rules by performing numerical simulations of colour-pattern time evolution with a probabilistic CA mathematical model. At each iteration of the simulation,

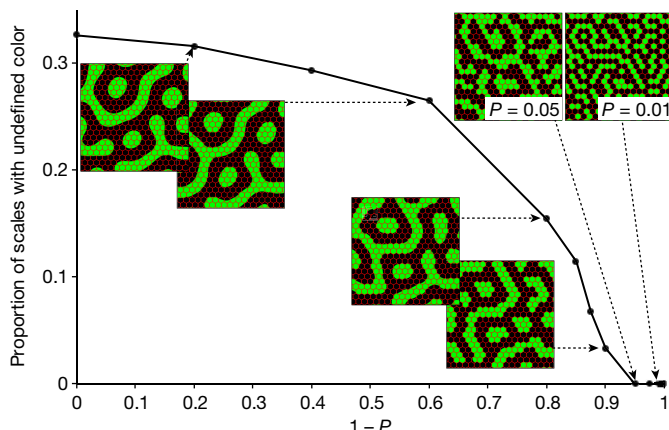


**Figure 5 | Sensitivity analysis.** A CA behaviour rapidly emerges from the continuous RD process when diffusion coefficients are reduced by a factor  $1 - P > 0.8$  in the inter-scale regions. Insets indicate the steady-state pattern generated using the corresponding factor. Scales are considered of undefined colour if <90% of their elements have the same colour.

the colour of each scale is changed following relative probabilities taken from Fig. 4d. Boundary conditions are described in Methods. Iterating this process generates patterns whose visual aspects (Fig. 4e; Supplementary Video 3) and scale neighbour state distributions (Fig. 4f) are highly similar to those of real ocellated lizards. We note that the number of scales changing during the CA simulations (about 1,500) is similar to the number of scales changing on the real animal.

In an attempt to differentiate CA-simulated from real patterns, we tried to refine the discriminating power of scale neighbourhood state statistics by taking into account the spatial distribution of neighbours (Extended Data Fig. 3), that is, the 14 different cases of neighbourhood states, assuming a neighbourhood size of six and rotational isotropy. This statistic, as well as a pair correlation function (widely used in physics and spatial statistics<sup>34,35</sup>), did not allow the differentiation of real patterns from those generated with our CA simulations. However, one could argue that the real and simulated labyrinthine patterns might exhibit some degree of universality, that is, many statistical CA transition rules (with colour-change probabilities potentially very different from those shown in Fig. 4d) might generate patterns that cannot be distinguished from ocellated lizard real patterns. We tested this hypothesis by implementing a genetic algorithm to optimize colour-change probabilities using a bin-wise difference statistics on the scale neighbourhood spatial state distribution function (of the simulated versus real pattern) as the optimality criterion. All genetic algorithm searches systematically converged to shape distributions of scale colour change probabilities similar to those estimated from the real data, suggesting that other profiles of relative probabilities cannot generate ocellated lizard patterns.

These results indicate that the quasi-hexagonal lattice of mesoscopic scales on ocellated lizards is a CA that computes a pattern. This striking observation is difficult to reconcile with the paradigmatic pattern-generating mechanism of interactions among elements (the biological cells) at a spatial scale much smaller than that of the lizard skin mesoscopic appendages. In other words, we need to understand how microscopic interactions among chromatophores can simultaneously (1) explain homogeneous colours within a skin scale, (2) generate colour transitions at the border of scales, (3) translate mesoscopically into a CA rule, and (4) generate a macroscopic pattern.

### From continuous RD to discrete RD to CA

Interactions among melanophores, xanthophores and iridophores control the development of the striped colour pattern of zebrafish<sup>1,2,9,36,37</sup>. The generation of double-mutants showed that none of these

chromatophores alone can generate a pattern, while the absence of melanophores or xanthophores leads to abnormal patterns<sup>2</sup>. Mutant-based functional studies have also demonstrated that malfunction in short-range interactions (such as cell–cell adhesion and communication) impairs cell migration/differentiation and proper pattern formation<sup>37</sup>. On the other hand, little is known about the nature of the long-range interactions involved in skin colour patterning, although the long cellular projections of melanophores towards xanthophores seem to involve the Delta/Notch signalling pathway<sup>3</sup>.

An interaction network and a system of RD equations that integrate short- and long-range activations and inhibitions have been shown to accurately reproduce zebrafish patterns of wild-type and mutant lines<sup>2,9</sup>. Attempting to bridge the gap between the inferred mesoscopic CA behaviour of macroscopic skin colour evolution in the ocellated lizard and the RD formalism of chromatophore microscopic interactions, we modelled the formation of the adult lizard pattern using a system of differential equations (see Methods and Extended Data Fig. 4) derived from zebrafish data.

Conceptually, a continuous RD model (approximating microscopic interactions among chromatophores) cannot generate a discrete mesoscopic CA behaviour unless an additional spatial parameter is taken into consideration. Here, we propose that the dramatic difference of thickness between scale and inter-scale skin is a geometrical parameter that causes the microscopic RD-like mechanism to generate a mesoscopic CA. Indeed, skin thickness and densities of chromatophores are much decreased in inter-scale skin (Fig. 2a, b, d and e), suggesting that interactions (cell–cell contacts) are substantially reduced between scales compared to within scales, a situation equivalent to projecting a 3D layer of varying thickness onto a 2D surface. We implemented this parameter in a continuous model (that is, with about 350 discretization elements per skin scale) by reducing in the RD equations all diffusion coefficients (see Methods) specifically along the scale boundaries. Simulations were performed on a strictly hexagonal lattice with periodic boundary conditions to remove the nuisance parameters of near-hexagonality and boundary condition of the real scale lattice. Supplementary Videos 4 and 5 and Extended Data Fig. 5a show that this continuous RD model indeed generates a scale colour-switching behaviour: colour is homogeneous within scales and scale colour switches between black and green rather than maintaining intermediate values. A sensitivity analysis (Fig. 5) indicates that this CA behaviour rapidly emerges from the RD process when diffusion coefficients are reduced by a factor  $>80\%$  in the inter-scale regions.

The emergence of a scale colour-switching behaviour from the continuous RD model discussed above implies that the skin colour pattern in ocellated lizards behaves as a discrete RD system with each complete reptile scale acting as a discretization unit. This representation explicitly ignores RD within a scale but is not identical to a CA because, here: (1) the colour state of a scale is a continuous variable that can take any value between ‘black’ and ‘green’ (although it spends most of the time near one of the two states, occasionally switching quickly from one to the other) and (2) colour change is occurring according to RD equations (rather than being based on neighbourhood-dependent probabilistic rules in the CA).

To attempt a formal derivation of the continuous and discrete RD model parameters that generate identical behaviours, we reason that continuous RD equations on a Voronoi tiling (approximating the lizard skin scales) can be reduced to discrete RD equations on the corresponding Delaunay triangulation. We do so under the assumptions that reaction coefficients are essentially constant across the skin, while the diffusion coefficients ( $D$ ) are substantially lower between tiles than on tiles. We formally show (see Methods for the full mathematical derivation) that continuous RD equations with a large reduction (by a factor  $0 \leq 1 - P \leq 1$ ) of the diffusion coefficients at the scale edges (of length  $S$  and width  $\varepsilon$ ) reduce to discrete RD equations with diffusion coefficients adjusted to  $\frac{2P}{3\sqrt{3}S\varepsilon}D$ .

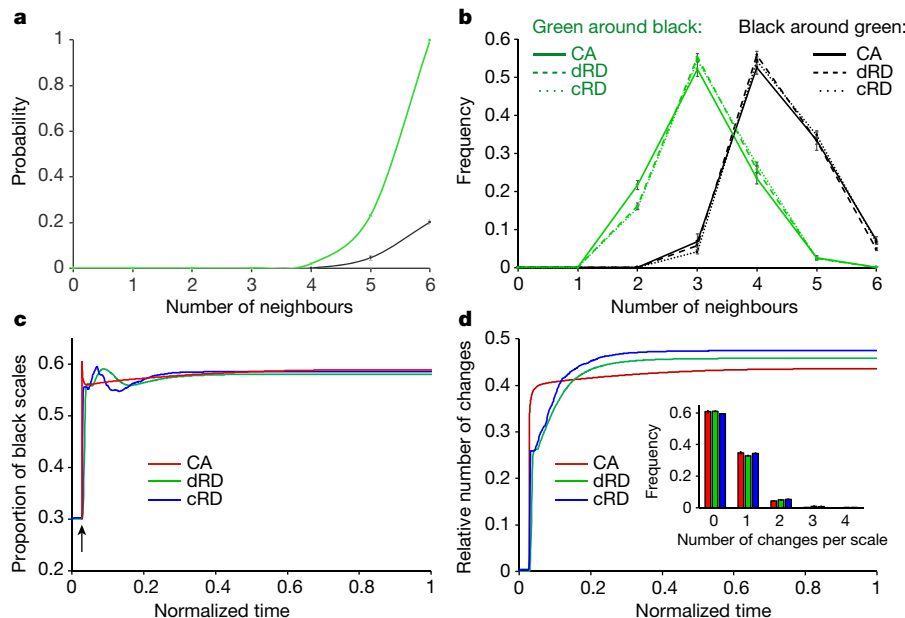


**Figure 6 | From RD to CA.** **a**, Colour-change probabilities for green scales (green line) and black scales (black line) as a function of nearest-neighbour scales matching their colour, estimated from discrete RD (dRD) simulations (mean  $\pm$  s.d. among 100 simulations). **b**, **c**, CA, discrete RD and continuous RD (cRD) modelling generate virtually undistinguishable steady-state neighbourhood distributions (**b**, mean  $\pm$  s.d. among 100 simulations) and steady-state proportions of black versus green scales (**c**, mean  $\pm$  s.d. among 100 simulations). The arrow in **c** indicates the

Finally, using the dynamic of colour changes in simulations implementing this discrete RD model, we experimentally determined the corresponding CA probability distributions (Fig. 6a). Crucially, all models (CA, discrete RD and continuous RD) yield, at steady state, highly similar neighbourhood distributions (Fig. 6b), macroscopic patterns and scale colour-switching behaviour (Supplementary Videos 3–8; Extended Data Fig. 5), as well as evolution of the green-to-black scale ratio (Fig. 6c). These analyses provide the first formal quantitative demonstration that a discrete RD, with a discrete von Neumann's CA behaviour, can be derived from Turing's continuous RD equations superposed on a lattice of borders at which diffusion is substantially reduced.

### Dynamics of scale colour change

Clearly, the number of scales changing colour slows down as the animal gets older. Although it could involve some sort of 'physiological/developmental ageing', this slow-down is probably an intrinsic property of the colour change mechanism itself. Indeed, given that green scales with many green neighbours and black scales with many black neighbours have a high probability of shifting colour (Figs 4d and 6a), the process causes a gradual increase in the number of neighbourhood states with very low probabilities of colour change (green scales with a low number of green neighbours and black scales with a low number of black neighbours; Fig. 4f and Fig. 6a and b). This should cause the pattern to converge and scales to almost stop changing colour even though the same probability distribution is effective throughout the life of the animal.

Testing this hypothesis quantitatively on real animals is difficult because their pattern did not reach steady state even though they were analysed over 3–4 years of their development. Indeed, the neighbourhood distribution still shifts moderately when CA simulations are carried on beyond 1,500 scale changes (Fig. 4f). In other words, the lizards we analysed will probably continue to change colour slowly for several years at a rate that will decrease as the neighbourhood distributions approach their steady state. We therefore used our hexagonal lattice

iteration at which the three models are aligned (that is, the moment colour changes start to occur). **d**, The colour-change slow-down observed on real ocellated lizards is an intrinsic property of the mechanism itself and is recapitulated by the CA, discrete RD and continuous RD simulations (means among 100 simulations). The inset shows the frequency distribution of changes per scale (mean  $\pm$  s.d. among 100 simulations) for CA, discrete RD and continuous RD.

with periodic condition to compare the dynamics of the CA, discrete and continuous RD models at steady state (Fig. 6d): in all cases, the dynamic of scale colour change drastically slows down then almost stops. We note that the CA is faster during its initial phase (very first iteration) because of the discrete time nature of this model.

### Scale size and developmental timing

The spatial length-scale of a pattern (that is, the average distance between pattern features, such as stripes or spots, generated by a RD system) is proportional to the square root of diffusion coefficients, if we study the RD system in the plane with constant RD coefficients (not reduced at the boundary of scales). In our model, diffusion coefficients are large enough for scales to have smaller size than features of the RD system in the plane, and thus scales take a uniform colour. For a pattern to appear within a scale, the diffusion coefficients must be reduced or the size of the scale must be increased beyond the spatial length scale of the pattern. This allows us to predict that a pattern should appear within large-enough scales. This prediction is confirmed by simulations (a pattern appears in scales whose size has been increased by a factor of about 2; Extended Data Fig. 6a) and by the frequent presence, in real ocellated lizards, of a pattern within the large scales at the base of the tail (Extended Data Fig. 6b). Finally, Fig. 6a shows that reduction of diffusion parameters at the border of lattice elements (representing skin scale borders) makes the pattern 'snap' to the size of the elements even if the corresponding length-scale of the pattern on a homogeneous domain (for example, within large scales) is larger than the size of an element.

The results reported here strongly suggest that the mesoscopic CA behaviour of ocellated-lizard-skin colour-pattern time evolution emerges from the superposition of the geometry of skin scales (that is, variation of skin thickness) with the paradigmatic nonlinear microscopic system of interactions among chromatophores. More specifically, the morphogenesis of scales establishes a skin thickness variation that seems necessary and sufficient to affect the cell interactions, effectively decoupling the behaviour of the RD equations within and among skin

scales and causing the emergence of a CA whose lattice elements are exactly superposed on the skin scales. However, many species of snakes and lizards do not show strictly ‘scale-dependent’ skin colour patterns (that is, the variation of colour does not systematically occur at the borders of scales). We anticipate that the parameters specifying a given level of scale-dependence in a species are associated with the relative developmental stages at which scale morphogenesis and colour patterns formation occur, the specific morphology of scales, as well as the size of the skin scales relative to the length scale of the colour pattern.

**Online Content** Methods, along with any additional Extended Data display items and Source Data, are available in the online version of the paper; references unique to these sections appear only in the online paper.

Received 3 October 2016; accepted 1 March 2017.

1. Inaba, M., Yamanaka, H. & Kondo, S. Pigment pattern formation by contact-dependent depolarization. *Science* **335**, 677 (2012).
2. Frohnhofer, H. G., Krauss, J., Maischein, H. M. & Nusslein-Volhard, C. Iridophores and their interactions with other chromatophores are required for stripe formation in zebrafish. *Development* **140**, 2997–3007 (2013).
3. Hamada, H. et al. Involvement of Delta/Notch signaling in zebrafish adult pigment stripe patterning. *Development* **141**, 318–324 (2014).
4. Irion, U. et al. Gap junctions composed of connexins 41.8 and 39.4 are essential for colour pattern formation in zebrafish. *eLife* **3**, e05125 (2014).
5. Fadeev, A., Krauss, J., Frohnhofer, H. G., Irion, U. & Nusslein-Volhard, C. Tight Junction Protein 1a regulates pigment cell organisation during zebrafish colour patterning. *eLife* **4**, e06545 (2015).
6. Turing, A. M. The chemical basis of morphogenesis. *Phil. Trans. R. Soc. Lond. B* **237**, 37–72 (1952).
7. Gierer, A. & Meinhardt, H. A theory of biological pattern formation. *Kybernetik* **12**, 30–39 (1972).
8. Kondo, S., Iwasa, M. & Yamaguchi, M. How animals get their skin patterns: fish pigment pattern as a live Turing wave. *Int. J. Dev. Biol.* **53**, 851–856 (2009).
9. Nakamasu, A., Takahashi, G., Kanbe, A. & Kondo, S. Interactions between zebrafish pigment cells responsible for the generation of Turing patterns. *Proc. Natl. Acad. Sci. USA* **106**, 8429–8434 (2009).
10. Kondo, S. & Miura, T. Reaction–diffusion model as a framework for understanding biological pattern formation. *Science* **329**, 1616–1620 (2010).
11. Kuriyama, T., Miyaji, K., Sugimoto, M. & Hasegawa, M. Ultrastructure of the dermal chromatophores in a lizard (Scincidae: *Plestiodon latiscutatus*) with conspicuous body and tail coloration. *Zoolog. Sci.* **23**, 793–799 (2006).
12. Cote, J., Meylan, S., Clober, J. & Voituron, Y. Carotenoid-based coloration, oxidative stress and corticosterone in common lizards. *J. Exp. Biol.* **213**, 2116–2124 (2010).
13. Weiss, S. L., Foerster, K. & Hudon, J. Pteridine, not carotenoid, pigments underlie the female-specific orange ornament of striped plateau lizards (*Sceloporus virgatus*). *Comp. Biochem. Physiol. B* **161**, 117–123 (2012).
14. Saenko, S. V., Teyssier, J., van der Marel, D. & Milinkovitch, M. C. Precise colocalization of interacting structural and pigmentary elements generates extensive color pattern variation in *Phelsuma* lizards. *BMC Biol.* **11**, 105 (2013).
15. Teyssier, J., Saenko, S. V., van der Marel, D. & Milinkovitch, M. C. Photonic crystals cause active colour change in chameleons. *Nat. Commun.* **6**, 6368 (2015).
16. Bagnara, J. T. & Matsumoto, J. in *The Pigmentary System: Physiology and Pathophysiology* (eds Nordlund, J. J. et al.) 11–59 (Blackwell, 2006).
17. Cott, H. B. *Adaptive Coloration in Animals* (Methuen, 1940).
18. Parker, G. H. Animal color changes and their neurohumors. *Q. Rev. Biol.* **18**, 205–227 (1943).
19. Bagnara, J. T., Taylor, J. D. & Hadley, M. E. The dermal chromatophore unit. *J. Cell Biol.* **38**, 67–79 (1968).
20. Nilsson Sköld, H., Aspengren, S. & Wallin, M. Rapid color change in fish and amphibians—function, regulation, and emerging applications. *Pigment Cell Melanoma Res.* **26**, 29–38 (2013).
21. Cross, M. & Greenside, H. *Pattern Formation and Dynamics in Nonequilibrium Systems* (Cambridge Univ. Press, 2009).
22. Murray, J. D. *Mathematical Biology* 3rd edn, Vol. 2 *Spatial Models and Biomedical Applications* (Springer, 2002).
23. Volpert, V. & Petrovskii, S. Reaction–diffusion waves in biology. *Phys. Life Rev.* **6**, 267–310 (2009).
24. Chopard, B. & Droz, M. *Cellular Automata Modeling of Physical Systems* 1st edn (Cambridge Univ. Press, 2005).
25. Deutsch, A. & Dormann, S. *Cellular Automaton Modeling of Biological Pattern Formation: Characterization, Applications, and Analysis* (Birkhäuser, 2005).
26. von Neumann, J. in *Cerebral Mechanisms in Behavior—The Hixon Symposium* (ed. Jeffress, L. A.) 288–326 (Wiley, 1951).
27. von Neumann, J. & Burks, A. W. *The Theory of Self-Reproducing Automata* (Univ. Illinois Press, 1966).
28. Wolfram, S. *A New Kind of Science* (Wolfram Media, 2002).
29. Martins, A. F., Bessant, M., Manukyan, L. & Milinkovitch, M. C. R<sup>2</sup>OBIE-3D, a fast robotic high-resolution system for quantitative phenotyping of surface geometry and colour-texture. *PLoS One* **10**, e0126740 (2015).
30. Furukawa, Y. & Ponce, J. Accurate camera calibration from multi-view stereo and bundle adjustment. *Int. J. Comput. Vis.* **84**, 257–268 (2009).
31. Woodham, R. J. Photometric methods for determining surface orientation from multiple images. *Opt. Eng.* **19**, 139–144 (1980).
32. Fricke, H. W. Behavior as part of ecological adaptation—in-situ studies in coral reef. *Helgoländer Wiss. Meer.* **24**, 120–144 (1973).
33. Booth, C. L. Evolutionary significance of ontogenetic color-change in animals. *Biol. J. Linn. Soc.* **40**, 125–163 (1990).
34. Hill, T. L. *Statistical Mechanics: Principles and Selected Applications* (McGraw-Hill, 1956).
35. Torquato, S. *Random Heterogeneous Materials: Microstructure and Macroscopic Properties* (Springer, 2002).
36. Mahalwar, P., Walderich, B., Singh, A. P. & Nusslein-Volhard, C. Local reorganization of xanthophores fine-tunes and colors the striped pattern of zebrafish. *Science* **345**, 1362–1364 (2014).
37. Singh, A. P. & Nusslein-Volhard, C. Zebrafish stripes as a model for vertebrate colour pattern formation. *Curr. Biol.* **25**, R81–R92 (2015).

**Supplementary Information** is available in the online version of the paper.

**Acknowledgements** We thank A. Debry and F. Montange for technical assistance with animals and B. Chopard for comments on the manuscript. A. Martins advised on R<sup>2</sup>OBIE scans. This work was supported by grants to M.C.M. from the University of Geneva (Switzerland), the Swiss National Science Foundation (FNSNF, grants 31003A\_140785 and SINERGIA CRSI13\_132430), and the SystemsX.ch initiative (project EpiPhysX). S.S. was supported by the ERC AG COMPASP, the FNSNF, the NCCR SwissMAP and the Russian Science Foundation.

**Author Contributions** M.C.M. initiated the ocellated lizard breeding colony, identified the CA behaviour and proposed that the CA emerges from the superposition of skin geometry with a continuous RD system. S.A.M. performed 3D scanning and histology. S.A.M. and L.M. performed 3D geometry and colour texture reconstructions. L.M. and S.A.M. performed the alignments among 3D scans and the colour assignment of scales. L.M. and M.C.M. performed the statistical analyses and numerical modelling on real lizard lattices (all code written by L.M.). A.F., S.S. and M.C.M. performed the analyses and simulations (all code written by A.F.) on hexagonal lattices. S.S. proposed the discrete RD model, performed the mathematical derivation of discrete RD parameters from the continuous RD models and advised on numerical simulations. A.F. proposed the CA probability numerical derivation. M.C.M. supervised the whole study and wrote the manuscript. All authors agreed on the interpretation of data and approved the final version of the manuscript.

**Author Information** Reprints and permissions information is available at [www.nature.com/reprints](http://www.nature.com/reprints). The authors declare no competing financial interests. Readers are welcome to comment on the online version of the paper. Publisher’s note: Springer Nature remains neutral with regard to jurisdictional claims in published maps and institutional affiliations. Correspondence and requests for materials should be addressed to M.C.M. (michel.milinkovitch@unige.ch).

**Reviewer Information** *Nature* thanks L. Edelstein-Keshet, T. Miura, C. Tarnita and T. Woolley for their contribution to the peer review of this work.

## METHODS

No statistical methods (such as power analysis) were used to predetermine sample size. The experiments were not randomized. The investigators were not blinded to allocation during experiments and outcome assessment.

**Animals and ethics statement.** Ocellated lizards were bred in Milinkovitch's laboratory, Department of Genetics and Evolution, University of Geneva, Switzerland. Maintenance of, and experiments on, animals were approved by the Geneva Canton ethical regulation authority (authorizations GE/82/14 and GE/73/16) and performed according to Swiss law. These guidelines meet international standards.

**Scanning, 3D-geometry reconstruction and texturing.** Starting from the newborn stage (about 2 weeks after hatching), animals were scanned for a period of 3–4 years and with a frequency of two weeks to four months (we increased the interval between scans as animals age because the rate of scale colour change decreases with age; Extended Data Table 1). The scanning was performed under anaesthesia (Sevoflurane with a mix of  $O_2$  at 0.6 litres per min and air at 0.4 litres per min) with R<sup>2</sup>OBIE-3D, a fast robotic high-resolution system for quantitative phenotyping of surface geometry and colour texture<sup>29</sup>. Each scan lasts less than 10 min for the acquisition of 54 to 145 high-resolution (36.3 megapixels) full-frame ( $36 \times 24$  mm) pictures. Note that scans in 2012 and before were performed manually using a Nikon D700 (full-frame, 12.1 megapixels), a tripod and a turn table. The 3D reconstruction and colour texturing were performed as described<sup>29,38</sup> and yielded texture and geometric resolutions of  $15\text{ }\mu\text{m}$  and  $40\text{ }\mu\text{m}$ , respectively. Briefly, we used (1) structure from motion (SFM<sup>30</sup>) methods, which derive the 3D geometry from the texture of pictures<sup>39–41</sup>, (2) photometric stereo (PS<sup>31</sup>) approaches, which measure high-frequency surface micro-geometry, or (3) a combination of SFM and PS. Additional details are available in ref. 29.

**Scales detection and neighbourhood connectivity.** For each animal and time point reconstructed using the SFM method, light scales were automatically detected using a brightness threshold, while dark scales and missing light scales were manually identified on the textured 3D model. For animals scanned with PS, the scales were detected semi-automatically as follows (Extended Data Fig. 1a). First, we computed local mean curvature at each vertex of the high-resolution 3D mesh using algebraic point set surfaces<sup>42</sup>. Second, we selected the vertices with curvature values larger than a manually selected threshold to separate scales from inter-scale skin. Third, we identified disconnected clusters of mesh vertices with high curvature and initialized scale positions as the centroids of these clusters. Fourth, each scale's first-ring neighbourhood connectivity information was retrieved using local 2D Voronoi diagrams. More specifically, for each scale, the 3D surface patch containing that scale and its 15 nearest-neighbour scales was locally mapped to 2D space, preserving the geodesic distances between the central scale and its 15 neighbours. The global Voronoi diagram was then generated by connecting the local diagrams while checking for one-to-one correspondences between direct neighbours. This approach proved to be very efficient, probably because each local 3D surface patch is approximately flat. A global, nearly conformal, 3D to 2D parameterization would have been much more complicated to implement and is not guaranteed to work as effectively as our local approach. Finally, the neighbourhood of scales was defined as the dual graph (Delaunay triangulation) of the Voronoi diagram. Note that the procedure generated about 1% of errors (misplaced, duplicated or undetected scales) such that manual inspection and corrections were required. As specular reflection on black scales tends to generate local spurious high curvature, the inferred scale position was sometimes off-centre of the real scale. To avoid that problem, we implemented a scale position refinement method (Extended Data Fig. 1b): neighbouring scale centres were connected with surface geodesic lines along which vertices with minimal curvature values (for example, saddle points) were identified, and each scale position was refined as the centroid of all its nearest-neighbour saddle points.

**Scale matching.** Once the network of scales has been identified for each developmental time point of a single animal, these networks are matched, that is, all scales are mapped from one time point to a referenced time point. This task is possible because we assume (and confirmed) that the number of scales is invariant for a given individual throughout its life. However, because the size of the animal, the positions of its body parts, and its skin pattern all change from scan to scan, the matching of scales at different time points is not a trivial task and requires geometric criteria. First, the 3D reconstructions of the two different time points (meshes A and B) are rigidly aligned (that is, translated, rotated and scaled) using the four limbs and the middle of the neck as morphological markers. Second, an initial scale  $S_i$  and one of its first neighbours  $S_j$  are manually identified on mesh A, and the corresponding two scales ( $S'_i$  and  $S'_j$ ) are manually identified on mesh B. We then compute the mean local translation, rotation and scaling factors required for aligning (mapping) these two scale pairs between meshes A and B, and we apply the same transformations to all first neighbours of scale  $S'_i$  (Fig. 1h and i). We then calculate the distances between corresponding scales and accept the alignment of  $S_i$  and  $S'_i$  and the alignment of its first neighbours if at least three of these distances

are below a specified threshold. Scale matching is then automatically propagated using the same procedure for each already mapped scale, and the process is iterated until all scales are matched between the two time points (Fig. 1j). Note that, at each iteration, already-mapped scales are used to compute the mean translation, rotation and scaling factors applied to all (mapped and not-yet-mapped) first-neighbour scales. Hence, the process can be viewed as an alignment that uses local rigid and global non-rigid deformations. Scales that have failed mapping are marked for manual correction.

**Scale colour detection.** Scale colour assignment is performed independently for each animal and each time point. First, the average colour of the 49 pixels in a  $7 \times 7$  pixel window around each marked scale position is computed. Second, blue scales are identified using hue, saturation and value (HSV) thresholding based on the observed HSV values of ten manually selected blue scales. Then, all other scales are separated into two clusters ('black' and 'green' scales) using vector quantization<sup>43</sup> performed in the 'laboratory colour' space (which is more perceptually uniform than HSV and most other colour spaces). Let us define the distances from a specific colour to the centre of each of the two clusters as  $d_1$  and  $d_2$ . A scale is marked with the colour it is the closest to if  $|d_1 - d_2| > 0.4(d_1 + d_2)$ ; otherwise it is considered equidistant from the two clusters and is marked as 'ambiguous'. In other words, a scale colour is ambiguous if  $d_1$  and  $d_2 > 0.3(d_1 + d_2)$ . Note that scales can be marked as ambiguous owing to (1) skin damage or (2) the presence of highlights or (3) being brownish, that is, an intermediate colour during the transition between black and green states. Ambiguity is lifted by comparing the problematic scale at the corresponding time point with the next time point at which that scale has an unambiguous colour. Scales remaining ambiguous are checked manually. For the most juvenile stages, we use four clusters—white, light-brown, dark-brown, and black—of which the first two were classified as 'green' and the other two as 'black'. Finally, all scales changing colour (from 'black' to 'green' or vice versa) were marked and all colour changes were visually confirmed.

**Scale colour pattern statistics.** The neighbour-state distribution histograms  $H(n)$  (for example, Figs 3b and 4f) are computed by counting how many green scales have  $n_B$  black first neighbours or how many black scales have  $n_G$  green first neighbours (since the majority of scales have six first neighbours, the histograms of green around green scales and black around black scales are essentially mirror distributions of the ones discussed above). The 'neighbour case distribution statistics'  $H(i)$  is the refined version of the neighbour state distribution where, apart from counting the number of first-neighbour scales with a specific colour, we also consider their spatial distribution, assuming rotational isotropy (counting symmetrical cases as one case, hence generating 14 different cases for six neighbours; Extended Data Fig. 3). Finally, a pair correlation statistic was estimated using geodesic distances and assuming isotropic point distribution<sup>44</sup>.

**Estimating scale colour change probabilities from real lizards.** Given a scale network with connectivity information, we define a set of changing probabilities  $p_G(n_G)$  and  $p_B(n_B)$  for green and black scales, respectively, where  $n_G$  is the number of first-neighbour green scales around a green scale, and  $n_B$  is the number of first-neighbour black scales around a black scale. We estimate  $p_G(n_G)$  and  $p_B(n_B)$  using the time series of scale colour change (over three years) in three ocellated lizard individuals (Fig. 4d). For each successive time points ( $t_i$  and  $t_{i+1}$ ), we compute (1)  $N_G(n_G)$ , the number of green scales at time  $t_i$  with  $n_G$  green nearest neighbours, and  $N_B(n_B)$ , the number of black scales with  $n_B$  black nearest neighbours, as well as (2)  $dN_G(n_G)$  and  $dN_B(n_B)$ , that is, the number of corresponding green and black scales changing colour between  $t_i$  and  $t_{i+1}$ . Hence, the absolute probability value for a green scale, with  $n_G$  green nearest neighbours, to become a black scale is  $p_G(n_G) = dN_G(n_G)/N_G(n_G)$ . The corresponding probabilities for black scales to become green are computed as  $p_B(n_B) = dN_B(n_B)/N_B(n_B)$ . The probability distribution is then estimated as a fitted cubic function ( $p(n) = an^3$ ) on the raw data (Extended Data Fig. 2a). Note that probability values are not computed when less than five scales are changing between two time points. For example, the number of green scales with more than five green neighbours can be too small for some time points. In that case, we estimate the corresponding missing probabilities by extrapolating the cubic function fitted on the reliable points (corresponding to lower values of  $n$ ). Given that all these distributions have the same shape, we normalize the absolute probabilities such that:

$$\sum_{n_G=0}^8 p_G(n_G) = 1$$

and

$$\sum_{n_B=0}^8 p_B(n_B) = 1$$

These relative probabilities were then used in the CA simulations on real lizard quasi-hexagonal lattices (Fig. 4e and f).

**CA simulations of pattern evolution on the lattice of scales.** We performed numerical simulations of colour pattern time evolution with a probabilistic CA mathematical model where the colour state of a scale at time  $t+1$  is a function of the state of its neighbours at time  $t$ ; this function corresponds to the relative probabilities computed above (Fig. 4d; Extended Data Fig. 2). More formally, we consider a 2D lattice of polygonal ‘cells’ (here representing skin scales) where each cell  $c$  exhibits one of two states  $S(c, t) = \{G, B\}$  at times  $t = 0, 1, 2, \dots$ . The time evolution of scales is defined by  $S(c, t+1) = R_G(n_G)$  and  $S(c, t+1) = R_B(n_B)$  for green and black scales, respectively.  $R_G$  and  $R_B$  make the scale switch colour with probabilities  $p_G(n_G)$  and  $p_B(n_B)$  taken from the distributions shown in Fig. 4d and in the inset of Fig. 4d, respectively.

We also tried the following alternative algorithm (which gave very similar results to the CA algorithm above) where, for every  $n_G = 0$  to  $\max_n n_G = 8$ , we randomly pick  $p_G(n_G)N_G(n_G)$  green scales and change their state to ‘black’ and, similarly, for every  $n_B = 0$  to  $\max_n n_B = 8$ , we randomly pick  $p_B(n_B)N_B(n_B)$  black scales and change their state to ‘green’. As discussed above,  $N_B(n_B)$  is the total number of black scales with  $n_B$  first-neighbour black scales and  $N_G(n_G)$  is the total number of green scales with  $n_G$  first-neighbour green scales.

The initial condition before starting a simulation corresponds to the pattern of a real ocellated lizard at an early time of its post-hatching development. Scales at the border of the network were kept invariant in colour. The simulation is stopped when the simulated pattern is closest (using the bin-wise difference statistics on the ‘neighbour case distribution’  $H(i)$ ) to the pattern observed on a real adult ocellated lizard; note that it requires a number of iterations causing about 1,500 scales to change colour, that is, the approximate number of scales that change colour in a real ocellated lizard during its first three years of life.

**Genetic algorithm optimization of the scale colour change probabilities.** We derived scale colour change probabilities from time series of scale colour changes in actual ocellated lizards (see above). To test whether other probability distributions would generate similar skin colour patterns, we also used a genetic algorithm to optimize colour-change probabilities with the bin-wise difference statistics (on the distribution  $H(i)$ ) as the fitness function. Using an Evolving Objects library<sup>45</sup>, we mutate  $p_G(n_G)$  and  $p_B(n_B)$  (model parameters) with a combination of three different operators (used with equal rates): (1) one model parameter is randomly selected and its value is changed with uniform probability using a rectangular sliding window of width 0.02; (2) all parameters are changed using the same procedure as in (1); and (3) all parameters are changed using a Gaussian distribution probability ( $\sigma = 0.3$ ). An alternative, self-adaptive mutation strategy was also used with the parameters of the Gaussian distributions being mutated<sup>45</sup>. The colour-change probability parameters were constrained in the (0, 1) range, but their sum was not forced to be 1.

Unconstrained genetic algorithm searches systematically converged to shape distributions of scale colour change probabilities similar to those estimated from the real data. We also performed exhaustive genetic algorithm searches while constraining  $p_G(n_G)$  and  $p_B(n_B)$  within the interval of their observed mean value  $\pm 2\text{s.d.}$ . This generated optimal distributions (that is, with smallest bin-wise difference statistics on the case distribution  $H(i)$ ) shown as dotted lines in Fig. 4d and used for CA simulations (Fig. 4e and f; Supplementary Video 3).

**The reaction–diffusion model.** It has been widely shown<sup>6,21–23,46,47</sup> that the nonlinearity of RD equations generates various patterns at a specific spatial scale. Experiments in zebrafish<sup>9</sup> suggest that melanophores and xanthophores dominate the process of pattern generation; hence, the iridophores are ignored in the model illustrated in Extended Data Fig. 4. This model is then represented by the following system<sup>9</sup> of nonlinear partial differential equations:

$$\begin{aligned} \frac{\partial u}{\partial t} &= F(u, v, w) - c_u u + D_u \nabla^2 u \\ \frac{\partial v}{\partial t} &= G(u, v, w) - c_v v + D_v \nabla^2 v \\ \frac{\partial w}{\partial t} &= H(u, v, w) - c_w w + D_w \nabla^2 w \\ F(u, v, w) &= \begin{cases} 0 & : c_1 v + c_2 w + c_3 < 0 \\ c_1 v + c_2 w + c_3 & : 0 \leq c_1 v + c_2 w + c_3 \leq F_{\max} \\ F_{\max} & : F_{\max} < c_1 v + c_2 w + c_3 \end{cases} \\ G(u, v, w) &= \begin{cases} 0 & : c_4 u + c_5 w + c_6 < 0 \\ c_4 u + c_5 w + c_6 & : 0 \leq c_4 u + c_5 w + c_6 \leq G_{\max} \\ G_{\max} & : G_{\max} < c_4 u + c_5 w + c_6 \end{cases} \\ H(u, v, w) &= \begin{cases} 0 & : c_7 u + c_8 v + c_9 < 0 \\ c_7 u + c_8 v + c_9 & : 0 \leq c_7 u + c_8 v + c_9 \leq H_{\max} \\ H_{\max} & : H_{\max} < c_7 u + c_8 v + c_9 \end{cases} \end{aligned}$$

The first right-hand-side term ( $F, G, H$ ) of each of the three partial differential equations represents interactions among the chromatophores, whereas ‘decay’ and ‘diffusion’ processes correspond to the second and third terms, respectively. The first ( $u$ ) and second ( $v$ ) components represent the densities of melanophores and xanthophores, respectively. The variables  $u$  and  $v$  also represent the densities of the short-range factors (with diffusion coefficient  $D_u = D_v$ ) expressed by their corresponding chromatophore type. The third component ( $w$ ) represents a long-range factor (diffusion coefficient  $D_w$  much larger than  $D_u$  and  $D_v$ ) produced by melanophores only. Density units are unspecified. The signs of the variables  $c_1, c_2, c_4, c_5, c_7$  and  $c_8$  are constrained by the cell interaction model shown in Extended Data Fig. 4. ‘Decay’ terms model cell behaviours such as differentiation, division and death while ‘diffusion’ represents cell movements and the production of long-range cellular projections.

#### Hexagonal lattice and continuous-to-discrete RD model formal derivation.

Although, for simplicity, we assume that the scales form an idealized hexagonal lattice with edge length  $S$ , we note that the effects of a particular graph are unessential to our reasoning. We approximate the continuous RD equations by their discretization to vertices of a square lattice with a sufficiently small edge length  $\varepsilon$  such that the RD system is essentially unchanged, with the same coefficients. The only difference is that the Laplacian is replaced by its discrete counterpart:

$$\nabla^2 u(x) = \sum_{x'} (u(x') - u(x))$$

where  $x'$  is a neighbour of  $x$ . The diffusion coefficients are changed by a factor of  $\varepsilon^{-2}$ , so the diffusion term becomes

$$\sum_{x'} \varepsilon^{-2} D_u (u(x') - u(x))$$

To account for smaller diffusion coefficients at the border of scales, we assume that the diffusion is changed by a factor  $P$  (that is, slower when  $P < 1$ ) in an  $\varepsilon$ -wide strip between scales, which in our discretization corresponds to a diffusion term of

$$\sum_{x'} \varepsilon^{-2} D_u P(xx') (u(x') - u(x))$$

where  $P(xx') = 1$  if the edge  $xx'$  does not intersect the boundary of a tile, and  $P(xx') = Psin(\theta)$  if the edge  $xx'$  intersects the boundary of a tile at an angle  $\theta$ . As explained below, the factor  $\sin(\theta)$  is needed for normalizations since edges at different angles are intersected with different frequencies.

Now we can derive the discrete RD equations on the Delaunay triangulation formed by the centres of the hexagons. We denote by  $H$  a hexagon with a centre  $z$ , and by  $z'$  we denote the centres of neighbouring hexagons. The discrete Laplacian on the Delaunay triangulation is given by

$$\nabla^2 U(z) = \sum_{z'} (U(z') - U(z))$$

We define the functions  $U, V$  and  $W$  at the centre  $z$  of a hexagon  $H$  as the averages of the corresponding functions on the vertices of the square lattice inside  $H$ . Note that the number of vertices of the square lattice inside  $H$  is approximately the area of  $H$  divided by  $\varepsilon^2$ , that is,  $\frac{3\sqrt{3}S^2}{2\varepsilon^2}$ , so  $U(z) = \frac{2\varepsilon^2}{3\sqrt{3}S^2} \sum_{x \text{ inside } H} u(x)$ .

We differentiate  $U$  in time, and on the equation above we plug in the RD equation on the square lattice, where  $x$  is inside hexagon  $H$  and  $x'$  is a neighbour of  $x$ :

$$\begin{aligned} \frac{\partial U(z)}{\partial t} &= \frac{2\varepsilon^2}{3\sqrt{3}S^2} \sum_x \frac{\partial u(x)}{\partial t} \\ &= \frac{2\varepsilon^2}{3\sqrt{3}S^2} \sum_x \left( F(u(x), v(x), w(x)) - c_u u(x) \right. \\ &\quad \left. + \sum_{x'} \varepsilon^{-2} D_u P(xx') (u(x') - u(x)) \right) \\ &= \frac{2\varepsilon^2}{3\sqrt{3}S^2} \sum_x (F(u(x), v(x), w(x)) - c_u u(x)) \\ &\quad + \frac{2\varepsilon^2}{3\sqrt{3}S^2} \sum_x \sum_{x'} \varepsilon^{-2} D_u P(xx') (u(x') - u(x)) \end{aligned}$$

Using the assumption that the functions  $u, v$  and  $w$  are essentially the same within each hexagon and so the average of  $F(u, v, w)$  over the hexagon is approximately equal to  $F(U, V, W)$  at its centre, we can simplify the first ‘reaction’ terms in the last expression to

$$\frac{2\varepsilon^2}{3\sqrt{3}S^2} \sum_x (F(u(x), v(x), w(x)) - c_u u(x)) \approx F(U(z), V(z), W(z)) - c_u U(z)$$

To deal with the ‘diffusion’ term, we note that, when the discrete Laplacian (written above as the sum of four differences) is summed over the hexagon, only the differences

across the boundary remain (each difference corresponding to an interior edge appears in the Laplacian term for its endpoints with opposite signs and so cancels out—the discrete analogue of Green's theorem), thus

$$\begin{aligned} & \frac{2\varepsilon^2}{3\sqrt{3}S^2} \sum_x \sum_{x'} \varepsilon^{-2} D_u P(xx')(u(x') - u(x)) \\ &= \frac{2}{3\sqrt{3}S^2} D_u \sum_{xx'} P(xx')(u(x') - u(x)) \end{aligned}$$

where  $xx'$  goes across a side of  $H$ . Now, consider a side of hexagon  $H$  separating it from hexagon  $H'$  with a centre  $z'$ , and suppose that it intersects some edge  $xx'$  at an angle  $\theta$ . Then

$$P(xx')(u(x') - u(x)) \approx P \sin(\theta)(U(z') - U(z))$$

Moreover there are about  $S \sin(\theta)/\varepsilon$  edges parallel to  $xx'$  intersecting this side, so their combined input into the expression above is approximately

$$S \frac{\sin(\theta)}{\varepsilon} P \sin(\theta)(U(z') - U(z)) = SP \frac{\sin^2(\theta)}{\varepsilon}(U(z') - U(z))$$

Since orthogonal edges intersect the same side at an angle  $(\pi/2 - \theta)$ , their input is approximately

$$SP \frac{\sin^2(\pi/2 - \theta)}{\varepsilon}(U(z') - U(z))$$

with two orthogonal directions summing together to

$$\frac{SP}{\varepsilon}(U(z') - U(z))$$

Plugging it into our expression of the 'diffusion' term, we equate it to

$$\frac{2}{3\sqrt{3}S^2} D_u \sum_{z'} \frac{SP}{\varepsilon}(U(z') - U(z)) = \frac{2P}{3\sqrt{3}S\varepsilon} D_u \nabla^2 U(z)$$

where  $z'$  is a neighbour of  $z$  in the Delaunay triangulation. We conclude that the functions  $U, V, W$  approximately satisfy the following discrete RD equations on the Delaunay triangulation:

$$\frac{\partial U(z)}{\partial t} = F(U(z), V(z), W(z)) - c_u U(z) + \frac{2P}{3\sqrt{3}S\varepsilon} D_u \nabla^2 U(z)$$

Thus we have established that the continuous RD equations with a substantially reduced diffusion coefficients at the borders of tiles (here, skin scales) can be reduced to discrete RD equations, whose diffusion parameter is adjusted to  $\frac{2P}{3\sqrt{3}S\varepsilon} D_u$ .

Note that we use spatially discrete RD equations with continuous time. In our numerical simulations (see below), we can discretize time as well, substituting the time derivative by a discrete difference divided by the time step  $dt$ .

**Continuous and discrete RD model implementation.** As an initial condition, the colour pattern of a real ocellated lizard at an early stage of its post-hatching development (first frame of Supplementary Video 2) was projected on a regular lattice of 2,640 hexagons approximately matching the number of scales in each direction on the corresponding real (near-hexagonal) lattice of skin scales. The average number of pixels per hexagon was 293 and a hexagon's colour was set to green if more than 40% of its pixels were green; otherwise the hexagon's colour was set to black. This procedure generated a pattern with 30% black scales as on the corresponding real lattice of skin scales.

Continuous RD simulations were implemented on a  $2,000 \times 380$  square lattice with step  $\varepsilon$  using periodic boundary conditions. As discussed above, the difference of skin thickness inside the skin scales versus their borders was simulated by superimposing a regular hexagonal pattern (with hexagon side length  $S$ ) and reducing the diffusion coefficients at the boundaries of hexagons, that is, we multiply the Laplacian by a factor  $P \sin(\theta)$  at edges intersecting an hexagon boundary with angle  $\theta$ . Each lattice element is initialized with the colour of the hexagon it belongs to: either black or green, defined as  $(u, v, w) = (6.85, 0.09, 4.75)$  or  $(0.05, 5.35, 0.09)$ , respectively. The colour value of each lattice element is then separately randomized with a function  $\text{rand}(x) = \max(x + r, 0)$ , where  $r$  is uniformly sampled from the interval  $[-0.1, 0.1]$ . At each simulation iteration, the colour of an element is set to black if  $u - v > 0$ , otherwise it is set to green. The scale component densities are updated with Euler integration. Hexagons are considered of undefined colour if  $<90\%$  of their elements have the same colour. Simulations are stopped when all pixels satisfy the condition

$$|u(t-1) - u(t)| + |v(t-1) - v(t)| + |w(t-1) - w(t)| < 10^{-6}$$

Simulation parameters generating the result shown in Fig. 6b, c and d are:  $c_1 = -0.04, c_2 = -0.056, c_3 = 0.382, c_4 = -0.05, c_5 = 0, c_6 = 0.25, c_7 = 0.016, c_8 = -0.03, c_9 = 0.24, c_u = 0.02, c_v = 0.025, c_w = 0.06, F_{\max} = G_{\max} = H_{\max} = 0.5, D_u = D_v = 1.125, D_w = 12D_u = 13.5, dt = 0.015, P = 0.00889, \varepsilon = 1$  and  $S = 20/\sqrt{3}$ .

Using the formal mathematical derivation described above, the discrete RD simulations are performed with diffusion coefficients ( $D^d$ ) computed as

$$D_u^d = D_v^d = \frac{2P}{3\sqrt{3}S\varepsilon} D_u = 0.00033$$

and  $D_w^d = 12D_u^d = 0.00396$ .

Using these diffusion parameters (and the time step  $dt = 1$ ), as well as the reaction parameters, initial conditions and stopping criteria of the continuous model, the discrete model behaves very similarly to the continuous model (Fig. 6b, c and d).

**Numerical derivation of CA probability distributions from discrete RD.** Using the dynamic of colour changes in our discrete RD simulations, we experimentally determined the corresponding CA probability distributions (Fig. 6a). A scale colour is assigned to black if  $f(t) = u(t) - v(t) > 0$ , otherwise it is assigned to green. To compute the colour change probabilities for a black scale with  $n_B$  black neighbours and for a green scale with  $n_G$  green neighbours, we define the following four vectors that are updated as the simulation progresses:  $N_B(n_B)$  and  $dN_B(n_B)$  are the number of black scales with  $n_B$  black neighbours and the number of those that changed colour, respectively;  $N_G(n_G)$  and  $dN_G(n_G)$  are the number of green scales with  $n_G$  green neighbours and the number of those that changed colour, respectively. At the beginning of the simulation, we set  $N_B(i) = dN_B(i) = N_G(i) = dN_G(i) = 0$  for all  $i = 1, 2, \dots, 6$ . If a scale changed colour at time  $t$ , we find the time point  $t'$  when the previous colour change of that scale happened (we use  $t' = 0$ , if this is the first colour change). If the newly observed change is black to green, we increment  $N_B(n_B)$  for all  $n_B$  observed around that scale in the interval  $[t', t)$ . Furthermore,  $dN_B(n_B)$  is incremented if there is a time point  $t'' \in [t', t)$  at which the number of black neighbours around that scale was equal to  $n_B$  and  $\frac{\partial f(t'')}{\partial t} < -D_{\min}$ , where  $D_{\min}$  is a manually selected derivative threshold of 0.039. Similarly, when a green to black colour change occurs, we increment  $N_G(n_G)$  for all  $n_G$  observed around that scale in the interval  $[t', t)$ , and we increment  $dN_G(n_G)$  if there is a time point  $t'' \in [t', t)$  at which the number of green neighbours was  $n_G$  and  $\frac{\partial f(t'')}{\partial t} > D_{\min}$ . When the simulation stopping criterion is reached (at time  $t_{\text{End}}$ ), we again detect the time point  $t'$  for each scale. If a scale finished the simulation as green, we update  $N_G$  for all  $n_G$  that appeared around that scale in the interval  $[t', t_{\text{End}}]$ . If a scale finished as black, we perform the corresponding updates of  $N_B$ . Finally, we define the colour change probabilities of a black scale with  $n_B$  black nearest neighbours and of a green scale with  $n_G$  green neighbours as  $dN_B(n_B)/N_B(n_B)$  and  $dN_G(n_G)/N_G(n_G)$ , respectively. Figure 6b, c and d shows that CA numerical simulations using these colour-change probabilities (Fig. 6a; derived from the discrete RD model) generate neighbouring distributions and dynamics of colour change very similar to those obtained with the discrete RD and continuous RD models. CA simulations were performed with periodic boundary conditions and 100 consecutive iterations without scale colour change as a stopping criterion.

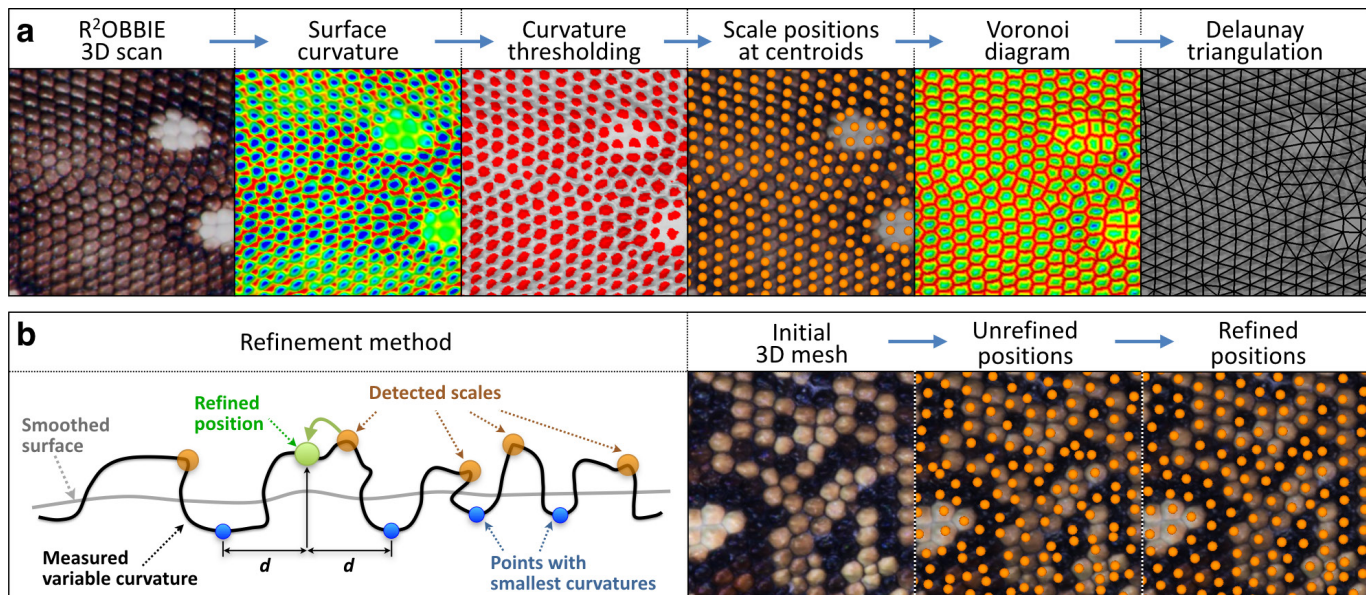
**Histology.** Adult and juvenile skins were processed as described<sup>48</sup> for haematoxylin and eosin (H&E) staining and as described in ref. 14 for TEM. In short, skin samples for H&E staining were fixed overnight in 4% paraformaldehyde before embedding in paraffin, sectioning (7-μm-thick sections), H&E staining and image acquisition (Pannoramic MIDI Slide scanner, 3D HISTECH). Skin samples for TEM were fixed overnight in 2% glutaraldehyde and 4% paraformaldehyde and fixed for 1.5 h in 1% osmium tetroxide and 0.8% K<sub>3</sub>Fe(Cn)<sub>6</sub>; samples were stained with 1% uranyl acetate for 2 h and embedded in epoxy resin (Epon); ultrathin (about 90 nm) transverse sections were cut with a diamond knife on a Leica UCT microtome and were placed on formavar-coated grids; the grids were then post-stained with uranyl acetate and lead citrate and viewed with a TecnaiTM G2 Sphera (FEI) TEM at 120 kV. Eight green scales and seven black scales were sectioned to observe the relative positions of the xanthophores, iridophores and dermal melanophores.

**The function of the pattern.** The functions of skin colour and colour patterns have been associated with, among others, thermoregulation, camouflage, and sexual selection<sup>11,14,15,49–59</sup>. The adaptive value of the colour pattern change in ocellated lizards is unknown, but might be associated to a shift in habitat or of predators between the juvenile and the adult stages (the main predators of *T. lepidus* are birds). Given that individuals of ocellated lizards acquire a labyrinthine green and black pattern around two to three years (that is, the age of sexual maturity), it also probably indicates reproductive status, although the most important signal for that function might be the blue ocelli on the flanks. The juvenile pattern could also act as a so-called 'intraspecific camouflage'<sup>32</sup> that reduces conspecific aggressiveness.

Finally, it is intriguing that the white ocelli (made of multiple skin scales) in the juvenile pattern are similar in size to the individual scales of the adult (see Fig. 1b and its inset). This motif size might be optimal for camouflage. Hence, one could argue that the combination of body growth and CA-based pattern evolution maintains a functional pattern length (spatial) scale at all ages of the animal.

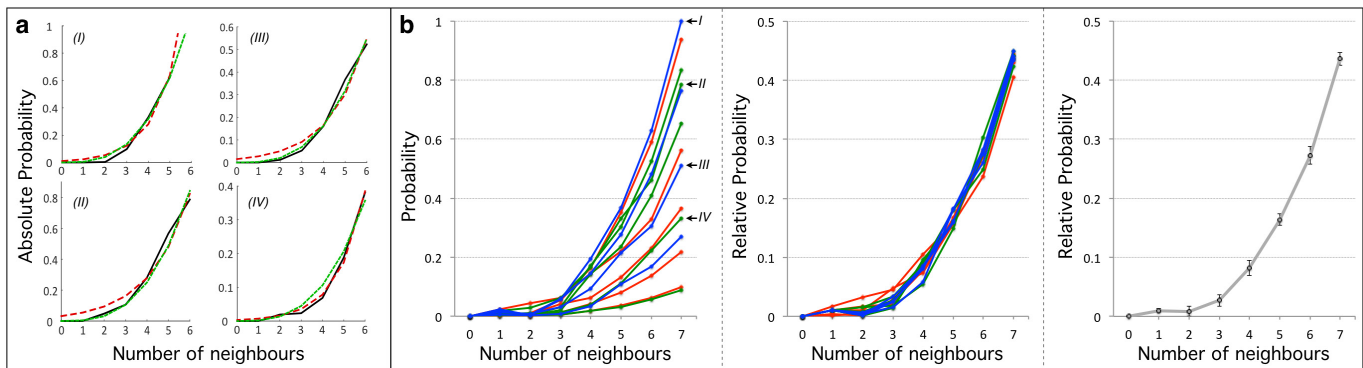
**Data availability.** Most data generated or analysed during this study are included in this published article and its Supplementary Information. Specific code and very large files with lizard 3D geometries are available from the corresponding author (M.C.M.) on reasonable request.

38. Milinkovitch, M. C. et al. Crocodile head scales are not developmental units but emerge from physical cracking. *Science* **339**, 78–81 (2013).
39. Hiep, V. H., Keriven, R., Labatut, P & Pons, J. P. Towards high-resolution large-scale multi-view stereo. In *IEEE Conf. on Computer Vision and Pattern Recognition (CVPR)* 1430–1437 (2009).
40. Yebin, L. et al. Continuous depth estimation for multi-view stereo. In *IEEE Conf. on Computer Vision and Pattern Recognition (CVPR)* 2121–2128 (2009).
41. Furukawa, Y. & Ponce, J. Accurate, dense, and robust multiview stereopsis. *IEEE Trans. Pattern Anal. Mach. Intell.* **32**, 1362–1376 (2010).
42. Guennebaud, G. & Gross, M. Algebraic point set surfaces. *ACM Trans. Graph.* **26**, 23 (2007).
43. Ahalt, S. C., Krishnamurthy, A. K., Chen, P. & Melton, D. E. Competitive learning algorithms for vector quantization. *Neural Netw.* **3**, 277–290 (1990).
44. Oztireli, A. C. & Gross, M. Analysis and synthesis of point distributions based on pair correlation. *ACM Trans. Graph.* **31**, 170 (2012).
45. Keijzer, M., Merelo, J. J., Romero, G. & Schoenauer, M. Evolving objects: a general purpose evolutionary computation library. *Lect. Notes Comput. Sci.* **2310**, 231–242 (2002).
46. Dhillon, D. S. J., Milinkovitch, M. C. & Zwicker, M. Bifurcation analysis of reaction diffusion systems on arbitrary surfaces. *Bull. Math. Biol.* **79**, 788–827 (2017).
47. Madzvamuse, A., Chung, A. H. & Venkataraman, C. Stability analysis and simulations of coupled bulk-surface reaction-diffusion systems. *Proc. R. Soc. A* **471**, 20140546 (2015).
48. Montandon, S. A., Tzika, A. C., Martins, A. F., Chopard, B. & Milinkovitch, M. C. Two waves of anisotropic growth generate enlarged follicles in the spiny mouse. *EvoDevo* **5**, 33 (2014).
49. Cooper, W. E. Jr & Greenberg, N. Reptilian coloration and behaviour. In *Biology of the Reptilia Vol. 18 Physiology E. Hormones* (eds Gans, C. & Crews, D.) 298–422 (Academic, 1992).
50. Hoekstra, H. E. Genetics, development and evolution of adaptive pigmentation in vertebrates. *Heredity* **97**, 222–234 (2006).
51. Gray, S. M. & McKinnon, J. S. Linking color polymorphism maintenance and speciation. *Trends Ecol. Evol.* **22**, 71–79 (2007).
52. Steffen, J. E. & McGraw, K. J. How dewlap color reflects its carotenoid and pterin content in male and female brown anoles (*Norops sagrei*). *Comp. Biochem. Physiol. B* **154**, 334–340 (2009).
53. Magalhaes, I. S., Mwaiko, S. & Seehausen, O. Sympatric colour polymorphisms associated with nonrandom gene flow in cichlid fish of Lake Victoria. *Mol. Ecol.* **19**, 3285–3300 (2010).
54. Rosenblum, E. B., Römler, H., Schöneberg, T. & Hoekstra, H. E. Molecular and functional basis of phenotypic convergence in white lizards at White Sands. *Proc. Natl Acad. Sci. USA* **107**, 2113–2117 (2010).
55. Brakefield, P. M. & de Jong, P. W. A steep cline in ladybird melanism has decayed over 25 years: a genetic response to climate change? *Heredity* **107**, 574–578 (2011).
56. Kronforst, M. R. et al. Unraveling the thread of nature's tapestry: the genetics of diversity and convergence in animal pigmentation. *Pigment Cell Melanoma Res.* **25**, 411–433 (2012).
57. Olsson, M., Stuart-Fox, D. & Ballen, C. Genetics and evolution of colour patterns in reptiles. *Semin. Cell Dev. Biol.* **24**, 529–541 (2013).
58. San-Jose, L. M., Granado-Lorencio, F., Sinervo, B. & Fitz, P. S. Iridophores and not carotenoids account for chromatic variation of carotenoid-based coloration in common lizards (*Lacerta vivipara*). *Am. Nat.* **181**, 396–409 (2013).
59. Spinner, M., Kovalev, A., Gorb, S. N. & Westhoff, G. Snake velvet black: hierarchical micro- and nanostructure enhances dark coloration in *Bitis rhinoceros*. *Sci. Rep.* **3**, 1846 (2013).



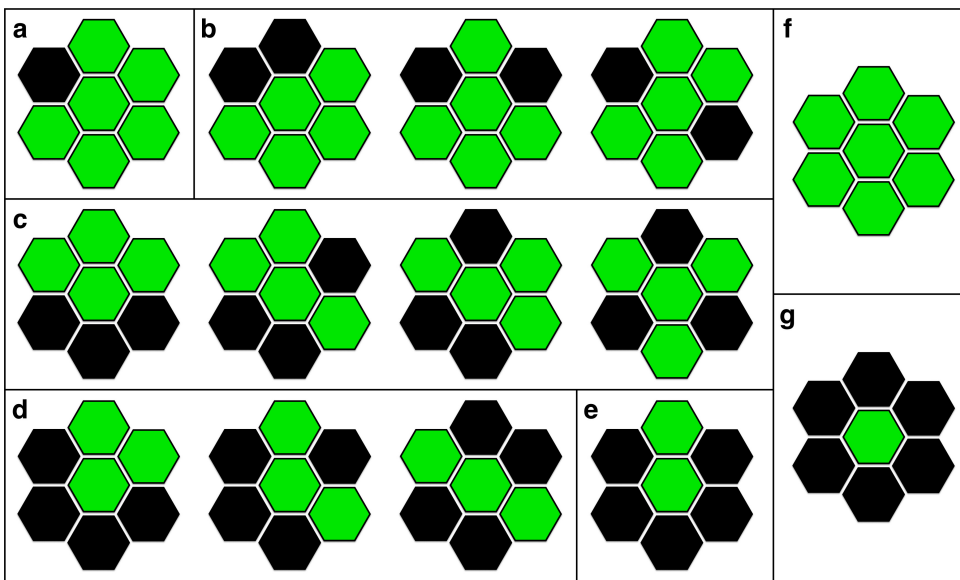
**Extended Data Figure 1 | Scale detection, positioning and identification of neighbourhood.** **a**, From left to right: the 3D high-resolution scan allows the curvature of the animal surface to be measured; curvature thresholding yields domains whose centroids define the positions of scales; and the latter are used to build the Voronoi diagram and its corresponding

Delaunay triangulation graph that identifies the neighbourhood of all scales. **b**, Each scale position is refined by moving it to the centroid of the corresponding polygon of smallest curvature (a 2D simplified representation is shown in the left panel; the refined position is at equal distances  $d$  from the two flanking points of smallest curvature).



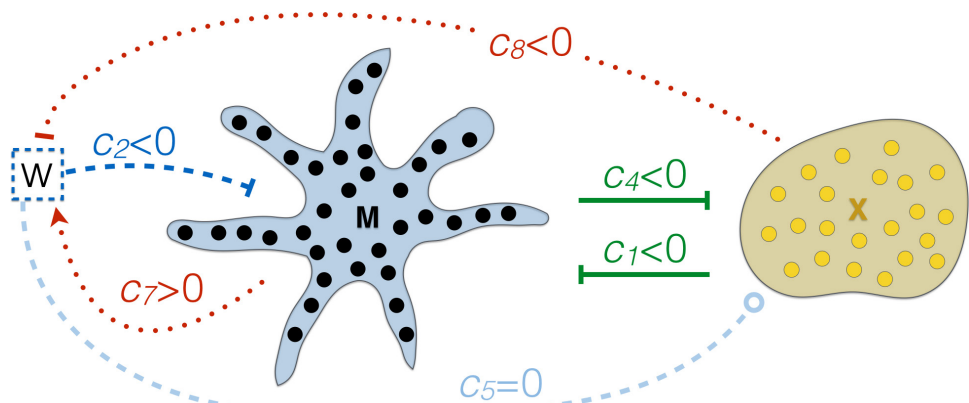
**Extended Data Figure 2 | Derivation of the scale colour change probability function.** **a**, Four examples of exponential (red) and cubic (green) fits of the raw data (black plain line) for green scales; the mean square difference per point is generally lower for the cubic than the exponential fit. The graph labelled (I) is an example of a time point for which the value for 6 neighbours is not available, so this value is estimated with the fitted curve. **b**, On the left is a polynomial cubic fit of the 13 colour change probability distributions corresponding to three different

individuals (blue, red and green curves) at different time points; the four curves labelled with Roman numbers correspond to the four graphs in **a**; all values are normalized with respect to the highest probability. In the middle is a normalized colour change probability distribution; each of the curves is normalized such that the sum of probabilities is 1. On the right the 13 normalized curves define a mean ( $\pm$ s.d.) colour change probability distribution.



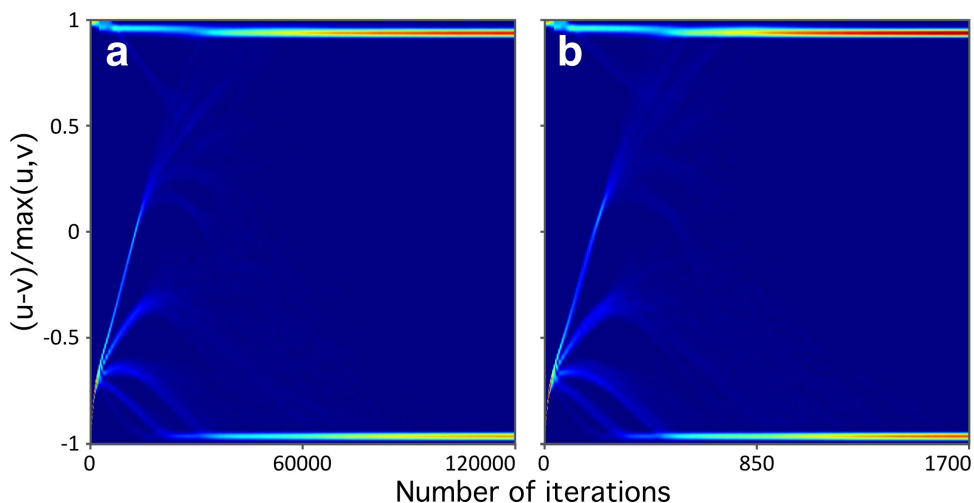
**Extended Data Figure 3 | The 14 possible first-ring neighbourhood states for a green scale in an hexagonal lattice.** Assuming rotational isotropy (counting symmetrical cases as one case), the central green scale can have one state with one black neighbour (a), three states with two

black neighbours (b), four states with three black neighbours (c), three states with four black neighbours (d), or one state with five or zero or six black neighbours (e, f and g).



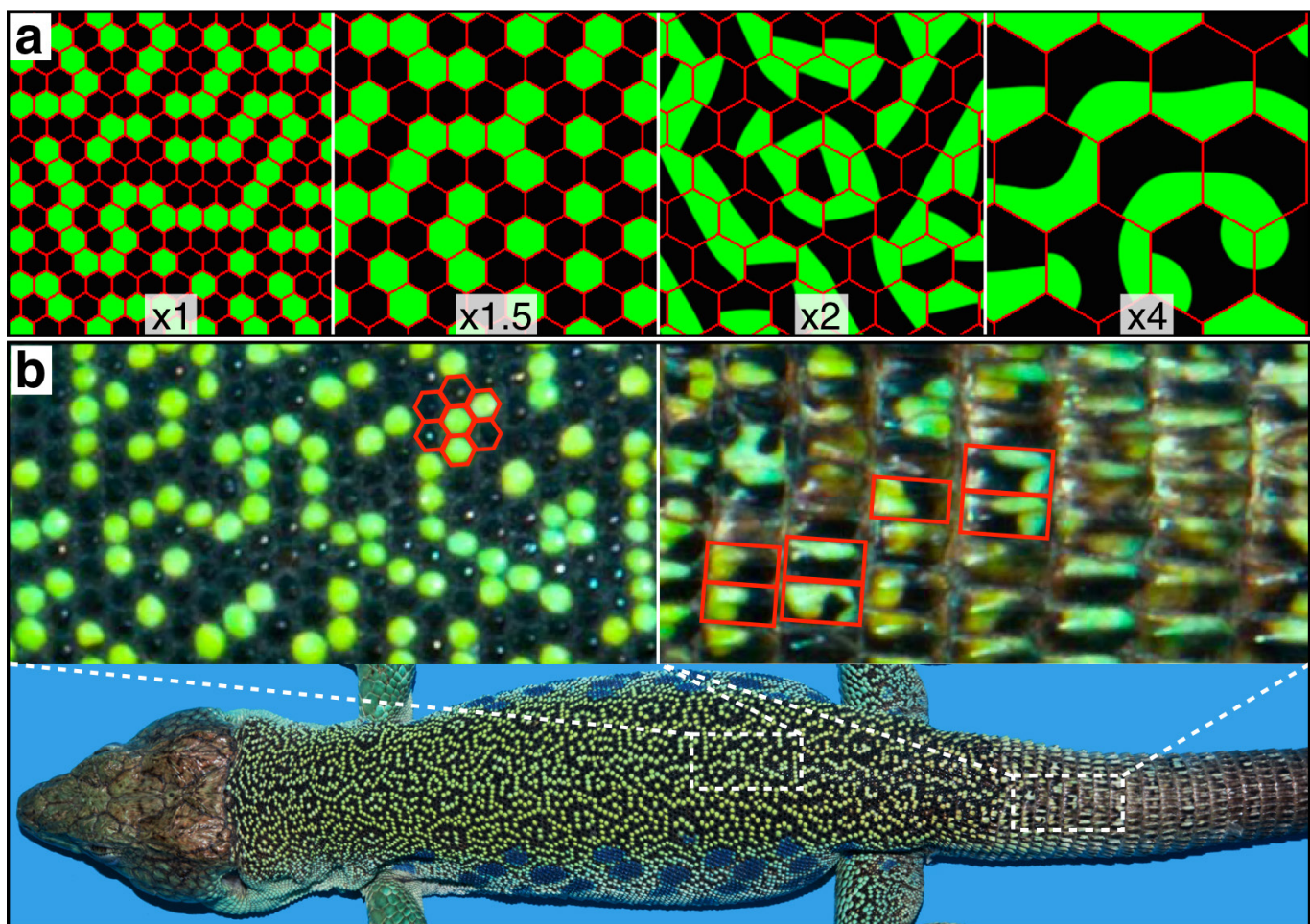
**Extended Data Figure 4 | Interactions between melanophores (M) and xanthophores (X).** The figure represents the model developed in ref. 9. Melanophores and xanthophores interact negatively with each other at short range (green arrows). W is the long-range inhibitor that affects melanophores (blue dashed arrow) but not xanthophores (light blue

dashed arrow and null parameter  $c_5$ ). W is modulated (red dotted arrows) positively by melanophores and negatively by xanthophores.  $c_1, c_2, c_4, c_5, c_7$  and  $c_8$  represent variables in the partial differential equations (see Methods).



**Extended Data Figure 5 | Switching of scale colour.** Density plots of skin scale colour (across all scales) for continuous (a) and discrete (b) RD simulations. For the continuous model, the colour of a hexagonal scale is computed as the mean among the  $(u - v)/\max(u, v)$  values of all elements

(pixels) in that hexagon. Both models generate a scale colour switching behaviour. Continuous RD simulations require smaller time steps than discrete RD, hence the higher number of iterations in the former.



**Extended Data Figure 6 | Skin colour pattern and scale size.** **a**, RD simulations with reduced diffusion at the scale borders show that a pattern appears within large-enough scales (magnification factors are indicated).

**b**, This prediction is confirmed by the absence of a colour pattern within the ocellated lizard body scales (left panel) but the presence of a colour pattern within most of the large tail scales (right panel).

**Extended Data Table 1 |** Eleven time points (TP0 to TP10), corresponding to age, expressed in weeks after hatching, at which three male ocellated lizards (LL09, LL10 and LL16) were scanned for colour texture and 3D reconstruction

	<b>LL09</b>	<b>LL10</b>	<b>LL16</b>
TP0	2 weeks	2 weeks	2 weeks
TP1	7 weeks	15 weeks	15 weeks
TP2	28 weeks	24 weeks	28 weeks
TP3	45 weeks	28 weeks	39 weeks
TP4	58 weeks	41 weeks	58 weeks
TP5	77 weeks	58 weeks	77 weeks
TP6	81 weeks	77 weeks	81 weeks
TP7	94 weeks	94 weeks	95 weeks
TP8	110 weeks	110 weeks	110 weeks
TP9	127 weeks	127 weeks	127 weeks
TP10	142 weeks	142 weeks	142 weeks